

A Chandra Observation of the Circinus Galaxy

David A. Smith and Andrew S. Wilson¹

*Department of Astronomy, University of Maryland, College Park, MD 20742;
dasmith@astro.umd.edu, wilson@astro.umd.edu*

ABSTRACT

We report on a recent *Chandra* ACIS-S observation of the Circinus galaxy. These observations confirm that the nuclear spectrum results from reflection of a hard X-ray continuum by “neutral” matter. The nuclear X-ray emission is extended by ~ 60 pc in the general direction of the optical “ionization cone”. An image in the Fe K α line has been made and shows that this emission extends up to 200 pc from the nucleus. There is also large-scale X-ray emission both along and perpendicular to the galaxy disk. Thermal plasma models for this extended gas indicate temperatures $kT \sim 0.6$ keV, though cooler photoionized gas is also possible. The X-ray emission from gas in the disk is probably associated with the starburst ring of radius 150–250 pc. The gas extending ~ 600 pc perpendicular to the disk is closely correlated with the high-excitation optical-line emission. In addition to its soft X-ray emission, we tentatively detect a hard component from the gas above the plane; this hard emission may represent nuclear X-rays scattered into our line of sight by electrons in the outflowing wind. Ten compact sources are found in the central kpc of the galaxy. The most luminous has an X-ray luminosity of $\simeq 10^{40}$ erg s^{−1} and seems to be an X-ray binary in the Circinus galaxy with a black-hole mass exceeding $80 M_{\odot}$.

Subject headings: galaxies: active — galaxies: individual: Circinus — galaxies: nuclei — galaxies: Seyfert — galaxies: starburst — X-rays: galaxies

1. Introduction

The Circinus galaxy is a large, nearby (4 ± 1 Mpc; Freeman et al. 1977) galaxy that harbors both a circumnuclear starburst and a Seyfert 2 nucleus. Evidence for an obscured Seyfert 1 nucleus is provided by the finding of a broad (FWHM $\simeq 3300$ km s^{−1}) H α line component in polarized

¹Adjunct Astronomer, Space Telescope Science Institute, 3700 San Martin Drive, Baltimore, MD 21218; awilson@stsci.edu

light (Oliva et al. 1998). The picture of an obscured Seyfert 1 nucleus is also supported by both the discovery of highly ionized gas extending along the minor axis of the galaxy, with a morphology that is reminiscent of the ionization cones seen in other Seyfert galaxies (Marconi et al. 1994), and the direct X-ray detection of the nucleus through a column density of $\sim 4 \times 10^{24} \text{ cm}^{-2}$ (Matt et al. 1999). The *ASCA* and *BeppoSAX* spectra below 10 keV shows both a flat continuum and intense Fe K α line emission, characteristic of the Compton reflection expected from cold gas illuminated by a hard ($\Gamma \simeq 1.7$) power-law continuum (Matt et al. 1996). Superposed on this spectrum are a number of emission lines from “neutral” and ionized states of Ne, Mg, Si, S, and Fe K β (Matt et al. 1996; Guainazzi et al. 1999). The energies and equivalent widths of the soft (0.5–3 keV) X-ray lines indicate that they cannot be produced in the material responsible for the Compton reflection, but must instead originate from highly ionized gas, possibly photoionized by the Seyfert nucleus (Sako et al. 2000). A recent *Chandra* High Energy Transmission Grating Spectrometer (HETGS) observation supports a two component, centrally-illuminated model (Sambruna et al. 2001b). Low ionization lines and the hard reflected continuum above ~ 2.5 keV originate from a cold gas in a compact region near (< 15 pc) the nucleus. High ionization lines and the softer, lower energy continuum arise in a highly ionized, more extended (50 pc) gas (cf. Netzer, Turner & George 1998). There is also large-scale X-ray emission towards the NW, which is roughly perpendicular to the major axis of the galaxy disk and in the direction of the high excitation gas evident in the optical images (Sambruna et al. 2001a). A number of compact X-ray sources are also seen.

Here we report on the results from a long ($\simeq 30$ ksec) observation of Circinus with the spectroscopic array of the Advanced CCD Imaging Spectrometer (ACIS-S; Garmire et al. 2000). These observations allow a study of the extended X-ray emission and compact X-ray sources with a higher signal to noise than available to Sambruna et al. (2001a). In this paper, we adopt a distance of 4 Mpc to the Circinus galaxy (Freeman et al. 1977), so $1'' = 19\text{pc}$.

2. Observations and Data Analysis

Since the nucleus of Circinus is known to be a strong X-ray source (e.g. Matt et al. 1996), we were concerned that “pile-up” could affect the *Chandra* observations. In order to measure the count rate of the nucleus, we first obtained a short observation (obsid 355) of Circinus on January 16, 2000. Single exposures with a 0.4s frame time were alternated with three exposures with a 3.2s frame time, the total integration time being $\simeq 1$ ks. This observation showed that the peak count rate per pixel for good grades taken in the 3.2s frame time mode was lower than that taken in the 0.4s frame time. Further, some 30% of the level 1 grades at the brightest pixel in the 3.2s frame time data were bad. Both of these effects indicate that pile-up is significant at the nucleus in a 3.2s frame time.

In order to obtain a spectrum of the nucleus which is free of pile-up, as well as a wide field deep observation, the science observations were taken in two exposures, both on March 14, 2000. Both exposures were taken with the nucleus of the galaxy at the aimpoint of the ACIS S3 chip. A

short ($\simeq 5$ ks) exposure (obsid 365) utilizing a subarray window of 128 rows on S3 and nominal frame time of 0.4s, was taken to obtain an “unpiled” spectrum of the nucleus. A longer ($\simeq 25$ ks) exposure (obsid 356) was taken with the default 3.2s frame time and chips I2, I3, S1, S2, S3, and S4 on, providing a deep integration of a wide field. We concern ourselves with only the central region of the galaxy, imaged on chip S3, in this paper.

Data reduction was performed using the latest version (1.1.5) of the *Chandra Interactive Analysis of Observations (CIAO)* software together with the level 2 events file, which contains only *ASCA* grades 0, 2, 3, 4, and 6. The level 2 events were gain corrected using calibration files appropriate for our observations. Times of bad aspect and high background were removed. Bad pixels and columns were excluded. The total good time intervals were 4913s and 24445s for the 0.4s and 3.2s frame-time exposures, respectively.

3. Results

3.1. The Central Region of Circinus

A *Chandra* ACIS image was extracted in the 0.5–8 keV band for the central $1'2 \times 1'2$ (1.35×1.35 kpc) region of the Circinus galaxy (Figure 1). The bright source at the center (source D) is the Seyfert nucleus. The *Chandra*–measured position of the nuclear source is $\alpha_x(2000) = 14^{\text{h}}13^{\text{m}}09^{\text{s}}94$, $\delta_x(2000) = -65^{\circ}20'21''.0$. This position is $1''.6$ away from the optical position ($\alpha_o(2000) = 14^{\text{h}}13^{\text{m}}09^{\text{s}}7 \pm 0^{\text{s}}1$, $\delta_o(2000) = -65^{\circ}20'21''.4 \pm 0''.7$; Freeman et al. 1977) and $0''.2$ away from the radio position ($\alpha_r(2000) = 14^{\text{h}}13^{\text{m}}09^{\text{s}}95 \pm 0^{\text{s}}02$, $\delta_r(2000) = -65^{\circ}20'21''.2 \pm 0''.1$; Greenhill 2001). The X-ray and radio positions are thus in agreement. The inner $31''.5 \times 31''.5$ (600×600 pc) region of the field is shown in more detail in Figure 2. The emission from the nucleus is clearly extended along the NW–SE direction. There are a total of 11 sources detected above a nominal 5σ threshold within the central $\simeq 1' \times 1'$ region using the WAVDETECT algorithm (distributed as part of the *CIAO* data analysis package). Table 1 gives the positions and background subtracted count rates for each source. The background was taken from source free regions surrounding each source. The count rates are for the combined 0.4s and 3.2s frame time data, except for sources D, F, and J, which are affected by pileup in the longer frame time data. We discuss the nuclear emission in Section 3.2, the large scale extended emission in Section 3.3, and the compact non-nuclear X-ray sources in Section 3.4.

3.2. The Nucleus

3.2.1. Extended Emission

A radial profile of the X-ray surface brightness was determined by extracting, from the unpiled short frame time observation, counts in circular annuli with widths 1 pixel ($0''.5$) centered on the

nucleus (Figure 3). The X-ray emission from compact sources close to the nucleus was excluded, and the background was estimated from a circular region $40''$ SW of the nucleus, which is free of large scale extended X-ray emission. The telescope PSF at 2 keV was calculated using the program MKPSF and file aciss1998-11-052dpsf3N0002.fits. We find the number of 0.5–8 keV counts within a radius of $3''$ is about twice that of the normalized telescope PSF, within the same radius.

The broad-band X-ray emission from the nucleus shows a bright core plus an extension of $\simeq 3\text{--}4''$ in position angle (p.a.) $\simeq 290^\circ$ (Figures 1, 2). This direction of X-ray extent is almost perpendicular to that of the galaxy disk (p.a. = 25° ; Maiolino et al. 1998). *HST* optical emission-line images (Wilson et al. 2000) show a compact **V**-shaped structure (possibly an “ionization cone”) extending $\simeq 2''$ to the NW (in p.a. = 316°) of the nucleus. The direction of elongation of the nuclear X-ray emission is close to that of the bright southern edge of this “**V**”, which lies in p.a. $\simeq 280^\circ$. Thus both the scale and direction of the nuclear X-ray extension are close to those of the optical emission-line “**V**”. Observations of Circinus in water maser emission reveal gas both in a warped, edge-on accretion disk and in outflow from the nucleus (Greenhill 2001). The mean p.a. of the maser outflow is 308° , which is also quite close to the direction of the X-ray extension in the nucleus.

The distribution of Fe $K\alpha$ line emitting gas was determined by extracting an image in the 6.2–6.5 keV band, which includes all of the Fe $K\alpha$ line emission, and subtracting the continuum at each location. This continuum was taken to be the average of the counts in the 5.9–6.2 and 6.5–6.8 keV bands. This continuum-subtracted line image was then convolved with a 2-D Gaussian profile of width $\sigma = 1$ pixel ($0''.5$) and the result is shown in Figure 4. The Fe $K\alpha$ emission of the nucleus is extended by a few arcsecs along the EW (in p.a. $\simeq 270^\circ$) direction, and there is a plume of emission extending some $10''$ from the nucleus towards the NW diffuse X-ray lobe (in p.a. $\simeq 330^\circ$; Figure 1). The EW extension lies along the southern edge of the “ionization cone” and the plume follows the eastern edge of the ionized gas $\sim 10''$ from the nucleus (see Figure 2 of Wilson et al. 2000). This raises the possibility that the extended Fe $K\alpha$ emission arises in neutral gas just outside the “cone”. We note that Fe $K\alpha$ emission is evident in the spectra of the nuclear extension, and the NW plume, and so these features in the Fe $K\alpha$ image are not artefacts of the continuum subtraction process.

3.2.2. Nuclear Spectrum

A spectrum was extracted from an elliptical region, with major axis in p.a. = 112.2° , and centered on the peak flux of the nucleus. The minor and major axes of the ellipse were $3''.12$ (60 pc) and $5''.22$ (100 pc) respectively. The X-ray emission from the two faint sources closest to the nucleus was excluded using two $1''.48 \times 1''.48$ rectangular regions centred on their peaks. The net (background subtracted) count rate from the nucleus was 0.33 cts s^{-1} for the short frame time observation, which does not suffer from pile-up. The data were initially fitted by a power-law continuum (photon spectral index Γ) absorbed by a column density (N_H), where the atomic cross-sections and abundances for the latter were taken from Morrison & McCammon (1983) and Anders & Grevesse (1989), respectively. We also included a Gaussian-shaped line to represent the Fe $K\alpha$

emission. This model (model 1) provides an unacceptable fit with $\chi^2 = 214.4$ for 127 degrees of freedom (d.o.f.), the best-fitting parameters being $\Gamma = 0.02_{-0.14}^{+0.13}$ and $N_{\text{H}} = 1.5 \pm 0.6 \times 10^{21} \text{ cm}^{-2}$ (the errors here, and elsewhere in this paper, are 90% confidence for one interesting parameter, $\Delta\chi^2 = 2.7$). We note that the column density in this model description is below the Galactic value of $N_{\text{H}}(\text{Gal}) = 3 \times 10^{21} \text{ cm}^{-2}$ (Freeman et al. 1977), indicating the model is unphysical. Fixing the column density at the Galactic value worsens the fit by $\Delta\chi^2 = 11.6$ (1 d.o.f.) and gives a larger photon index of $\Gamma \simeq 0.22$. Thus, we conclude that there is evidence in the ACIS data for soft X-ray emission in excess of the absorbed power-law (cf. Matt et al. 1996; Sako et al. 2000). The energy and equivalent width of the Fe K α emission line are 6.38 keV and ~ 3 keV, respectively. A hard ($\Gamma \sim 0$) power-law continuum and strong Fe K α emission were found in earlier *ASCA* (Matt et al. 1996; Sako et al. 2000) and *BeppoSAX* (Guainazzi et al. 1999) observations, and in the *Chandra* HETGS observation (Sambruna et al. 2001b). These properties are expected if we see the nuclear spectrum Compton reflected from the far side of a putative dense torus, and do not directly view the nucleus itself.

In addition to the Fe K α line at 6.38 keV, prominent emission lines are visible in the spectrum at ~ 0.9 , 1.2–1.3, 1.7–1.9, 2.3–2.5, and ~ 7.0 keV (Figure 5), corresponding to the neutral or ionized states of Ne, Mg, Si, S, and Fe K β . A large number of emission lines have been identified in the HETGS observation of Circinus (Sambruna et al. 2001b). These data have much higher spectral resolution than ours, and we decided to include the lines detected by Sambruna et al. (2001b) in our spectral model. Thus, the next step was to fit the data to a model (model 2) consisting of the Compton reflected continuum expected from a power-law spectrum (of photon index $\Gamma = 1.7$, a typical value for an unobscured Seyfert nucleus; cf. Matt et al. 1996; Guainazzi et al. 1999) incident on neutral, solar abundance material (as implemented in the PEXRAV model; see Magdziarz & Zdziarski 1995), a broad Gaussian-shaped line representing Fe K α emission, and narrow ($\sigma = 10$ eV) Gaussian emission lines at the energies given by Sambruna et al. (2001b). The inclination (to our line of sight) of the reflecting material was fixed at the angle-averaged value ($i = 63^\circ$), since the reflection spectrum below 10 keV is relatively independent of the inclination angle. The shape of the incident spectrum above 10 keV is important, even when considering measurements below this energy, because of the effects of Compton down-scattering; the power-law continuum was therefore taken to be exponentially cut-off with an e-folding energy of 150 keV, similar to that observed in other Seyfert galaxies (Zdziarski et al. 1995; Gondek et al. 1996). Finally, we added a thermal bremsstrahlung continuum to represent the soft X-ray emission (a power-law continuum of large photon index could have been used instead). All spectral components were assumed to be absorbed by the Galactic column density and a column intrinsic to the nucleus.

Model 2 (Table 2) gives an acceptable fit to the data for an intrinsic column of $N_{\text{H}} = 4.4_{-2.1}^{+4.7} \times 10^{21} \text{ cm}^{-2}$ and a thermal bremsstrahlung temperature of $kT_{\text{brems}} = 0.52_{-0.29}^{+0.41} \text{ keV}$ ($\chi^2 = 114.7$, 99 d.o.f.). The temperature of the thermal component agrees well with that found ($0.69_{-0.07}^{+0.05} \text{ keV}$) by Sako et al. (2000) in their collisionally ionized equilibrium model. The best-fitting energy, intrinsic width, and normalization of the Fe K α emission line are $6.382_{-0.010}^{+0.011} \text{ keV}$, $\sigma = 58 \pm 13 \text{ eV}$, and

$2.93^{+0.33}_{-0.39} \times 10^{-4}$ photons $\text{cm}^{-2} \text{sec}^{-1}$, respectively. Most of the line normalizations are consistent with those of Sambruna et al. (2001b), the exceptions being those at 1.471, 2.006, 4.758, 6.656, and 7.030 keV. The total efficiency curve of the back-illuminated S3 chip contains structures at the Al K-edge (1.55–1.56 keV) and the M-edge of iridium (~ 2 keV), which arise from X-ray absorption in the optical blocking filter and mirror surfaces respectively (Chartas et al. 2000). Thus, the lack of line emission in the ACIS spectrum at 1.471 and 2.006 keV may be due to inaccuracies in the response matrix at energies where the total efficiency of the detector is changing rapidly. The line present in the HETGS spectrum at 4.758 keV has a low signal to noise ratio, and our upper limit is consistent with the 1σ uncertainty of Sambruna et al. (2001b). The two other lines, at 6.656 and 7.030 keV, have significantly lower fluxes in the ACIS spectrum than in the HETGS spectrum. However, the close proximity of the 6.656 keV line to the strong Fe $K\alpha$ fluorescence line at 6.4 keV makes an accurate determination of the line flux difficult, and it is possible that some of the HETGS line flux may originate from regions outside our extraction area. Our measured flux of the Fe $K\beta$ line at 7.030 keV could be too low if an Fe K-edge is present in excess of that assumed in the continuum model.

3.3. Large Scale X-ray Emission

There is a considerable amount of diffuse X-ray emission in the Circinus field, extending hundreds of parsecs NE, SW and especially NW from the nucleus (Figure 1). The NE and SW extensions follow roughly the plane of the galaxy disk (p.a. $\simeq 25^\circ$; Maiolino et al. 1998), while that to the NW is approximately perpendicular to it. This can be seen in Figure 6, which is a superposition of the 0.5–8 keV X-ray emission (greyscale) on contours of an optical continuum image at 7000Å (Marconi et al. 1994). Astrometric coordinates were assigned to the optical image through a comparison between the positions of stars in this image and an *HST* I band image (Wilson et al. 2000). X-ray spectra were extracted from elliptical-shape regions centred on the SW and NW extended regions; we have excluded from the SW spectrum compact sources and extended X-ray emission close to the nucleus (Figure 7). Background spectra were taken from a circular region 40'' SW of the nucleus, where there is no large-scale extended X-ray emission from Circinus. Soft, faint, diffuse X-ray emission from our Galaxy is a possible contaminant of the background given the low Galactic latitude of Circinus ($b = -3.^\circ 8$; Freeman et al. 1977). However, similar results were obtained using background spectra taken from other long ACIS-S observations in which the discrete sources of X-ray emission had been excised². These observations are of “blank-sky”, were taken at the same focal plane temperature as our Circinus observations (i.e. -120°C), and the background spectra were extracted from the same regions of the chip as the source spectra in our Circinus observations.

In performing the spectral analysis of the extended X-ray emission, we have used both the

²See <http://hea-www.harvard.edu/~maxim/axaf/acisbg/> for further details regarding the ACIS background fields.

maximum-likelihood, or C-statistic (method 1; Cash 1979) and the χ^2 statistic (method 2). Method 1 does not require the data to be re-binned, and thus avoids potential loss of information on narrow spectral features. However, use of the C-statistic requires the background to be modelled (with simple power-laws and Gaussians) rather than subtracted directly, and there is no test for goodness of fit. The confidence intervals are calculated in the same way as for the χ^2 statistic, and are usually tighter for any given parameter (e.g. Nousek & Shue 1989). Method 2 requires the data to be binned so that there are a minimum of (typically) 20 counts per spectral bin, and the background is subtracted directly from the data. We find similar values for the best-fitting continuum parameters using the two methods, and so refer to only the method 2 results in the text. However, method 1 results give more precise measurements on the line features, and so these results are referred to when giving best-fit line energies, normalizations, and equivalent widths.

3.3.1. The NW region

We have modelled the extended emission in terms of combinations of hot thermal plasma and power-law models. A single component does not describe the spectrum of the NW extension. Therefore, the data were fitted to a two-component model consisting of thermal bremsstrahlung and a power-law continuum (model B+P). This model gave an acceptable fit to the data with $\chi^2 = 28.9$ for 22 d.o.f., the best-fitting parameters being given in Table 3. Several line features are evident in the spectrum (Figure 8), the most prominent being those at $1.775^{+0.025}_{-0.025}$ (consistent with Si VII–X K α) and $6.37^{+0.10}_{-0.06}$ keV (consistent with Fe II–XX K α). The line at 1.78 keV is close in energy to the Si K α fluorescence line in the background of the S3 chip (see Table 3 of Chartas et al. 2000). Thus, we consider whether this line might be an artefact left over from the background subtraction or modelling. The (background subtracted) flux of the 1.78 keV line in the data is $(8.8^{+4.9}_{-4.5}) \times 10^{-7}$ photons cm $^{-2}$ s $^{-1}$, whereas the flux of the Si K α line in the background spectrum (scaled to the area of the NW extension) is 6.3×10^{-9} photons cm $^{-2}$ s $^{-1}$. Therefore, it is unlikely that the line is a residual from the background subtraction or modelling. Replacing the thermal bremsstrahlung continuum with a MEKAL model (Mewe et al. 1995) gives a slightly better fit to the data for solar abundances (model M1+P; Table 3). However, the column density is below the Galactic value so the model is unphysical. A significant (at > 96% confidence) improvement in the fit is obtained for a metal abundance of $0.052^{+0.047}_{-0.023}$, and a column density consistent with the Galactic value (model M2+P; Table 3). A two MEKALS (both with solar abundances) model (model M1+M1; Table 3) gives a similar quality fit to the data as the M1+P model, but the column density is again well below the Galactic value. A significant (at > 97% confidence) improvement in the fit is obtained when we allow the metal abundance to vary from the solar value (model M2+M2, both MEKALS have the same metallicity, Table 3). However, the temperature of the hotter MEKAL component is very high ($kT_h = 80$ keV, which is the hottest temperature at which the model is tabulated) and unconstrained, making it impossible to distinguish the M2+M2 from the M2+P model. The temperature of the cooler MEKAL ($kT \sim 0.6$ keV) agrees well with the collisional ionization equilibrium model of Sako et al. (2000). The addition of a second MEKAL component

to either the M1+P or M2+P models does not significantly (at $\gtrsim 70\%$ confidence) improve the fit. The best fitting models in Table 3 have column densities consistent with the Galactic value ($N_{\text{H}}(\text{Gal}) = 3 \times 10^{21} \text{ cm}^{-2}$). This result is expected since the NW region lies on the near side of the Circinus galaxy disk, along the rotation axis. None of the models adequately reproduces the strength of the Fe K α line, whose observed equivalent width is $2.7^{+2.4}_{-1.9} \text{ keV}$.

In the M2+P model, the best-fit power-law photon index is $\Gamma = 0.0^{+0.5}_{-1.9}$, which is close to the value observed in the nuclear spectrum of Circinus. Of course, the spectral index of the hard power-law is very uncertain (Table 3); it is consistent with the observed value ($\Gamma \simeq 0.2$) for the nucleus, which we interpreted as a result of reflection from an optically thick torus, and marginally consistent ($\Delta\chi^2 \simeq 6$) with the putative unobscured index ($\Gamma = 1.7$). In evaluating the physical nature of this hard component, we first consider whether it might result from scattering of nuclear photons by the telescope mirrors. From estimates of the telescope PSF at 6.4 keV, some 0.25% of the photons from a point-like nucleus would fall within the extraction region used for the NW extension. The ratio of the 3–10 keV flux (which excludes most of the soft thermal X-ray emission) of the NW extension to that of the nucleus is $\simeq 0.5\%$, or twice that expected from the telescope PSF. We have also compared the hard flux of the NW extension with the flux in a region at the same distance from the nucleus where there is no detected diffuse emission from Circinus (e.g. towards the SE). The 3–10 keV count rates of the NW extension and a region to the SE with the same area are $(1.7 \pm 0.3) \times 10^{-3} \text{ cts s}^{-1}$ and $(1.2 \pm 0.2) \times 10^{-3} \text{ cts s}^{-1}$ respectively. Therefore, we tentatively conclude that the hard power-law component in the NW extension is real. A plausible interpretation is that this hard power-law component is nuclear flux scattered by electrons in an ionized gas above the plane of the galaxy. The flux and equivalent width of the Fe K α emission line in the NW extension are $(1.2^{+1.0}_{-0.8}) \times 10^{-6} \text{ photons cm}^{-2} \text{ s}^{-1}$ and $2.7^{+2.4}_{-1.9} \text{ keV}$, respectively. The true line flux will be smaller than this value, because the telescope PSF contributes $7.5 \times 10^{-7} \text{ photons cm}^{-2} \text{ s}^{-1}$ from Fe K α emission line in the nuclear spectrum. However, Fe K α emission lines of large equivalent width can readily occur if a small fraction of the nuclear emission is scattered by a warm “mirror” (Krolik & Kallman 1987; Band et al. 1990).

3.3.2. The SW region

A similar spectral fitting approach was adopted for the spectrum of the SW extension as that used for the spectrum of the NW region. Several lines are evident in the spectrum (Figure 9), the most prominent being the Fe K α and K β emission lines at $6.410^{+0.035}_{-0.027} \text{ keV}$ and $7.030^{+0.039}_{-0.035} \text{ keV}$ respectively. A two-component model consisting of a thermal bremsstrahlung plus power-law continuum (model B+P) provides a poor fit to the data with $\chi^2 = 42.5$ for 24 d.o.f. (the probability that the model describes the data and that χ^2 exceeds the observed value by chance is 1%); the best-fitting parameters are given in Table 4. Replacing the thermal bremsstrahlung continuum with a solar-metallicity MEKAL model gives a much better fit to the data (model M1+P, Table 4). A significant (at $> 99.5\%$ confidence) improvement in the fit is obtained for a metal abundance of

$0.088^{+0.052}_{-0.031}$ times solar (model M2+P, Table 4). A two MEKALS model (model M1+M1, each with solar metallicity) gives a worse fit to the data than does the M1+P model. Although a significant (at $> 99.7\%$ confidence) improvement in the fit is obtained when the metal abundance is allowed to vary (model M2+M2, both MEKALS are assumed to have the same metallicity, Table 4), the fit is worse than that for the M2+P model. Thus, we prefer the MEKAL plus power-law description of the SW extension. It is notable that all values of the absorbing column density in Table 4 exceed the Galactic column, indicating that significant absorption occurs within the disk of the Circinus galaxy. None of the models reproduce the strong Fe $K\alpha$ and Fe $K\beta$ lines.

Given the close proximity of the SW region to the nucleus, approximately 1% of the 3–10 keV flux of a point-like nucleus would fall within the extraction region used for the SW extension. The ratio of the (background subtracted) 3–10 keV count rates of the SW extension to that of the nucleus is $\simeq 1\%$, in agreement with that expected from the telescope PSF. Therefore, we conclude that the hard power-law component in the SW extension is not real but represents nuclear emission scattered by the telescope mirror. Finally, we note that the Fe $K\alpha$ emission line flux in the SW extension is $(2.1^{+1.6}_{-0.9}) \times 10^{-6}$ photons $\text{cm}^{-2} \text{s}^{-1}$, which is also consistent with the value expected from scattering of the strong nuclear Fe $K\alpha$ emission by the telescope mirror.

3.4. Compact X-ray Sources

Spectra were extracted using circular regions for each of the ten non-nuclear sources listed in Table 1. The radius of the extraction region was chosen to include all of the source flux above the background level, and ranged from $1.''2$ to $3.''0$. Background spectra were accumulated from annuli surrounding the source or, in the case of sources close to the nucleus, from circular regions the same distance from the nucleus as the source. Prior to spectral fitting, the source spectra were re-binned so that there were at least 20 cts bin^{-1} (sources B through K) or 10 cts bin^{-1} (source A). An absorbed power-law continuum provides an acceptable fit to each spectrum, and the best-fitting values of column density, N_{H} , and power-law photon index, Γ , are given in Table 5. The observed 2–10 keV fluxes range from 2.0×10^{-14} to 5.1×10^{-12} erg $\text{cm}^{-2} \text{s}^{-1}$, corresponding to an unabsorbed X-ray luminosity between 4.1×10^{37} and 10^{40} erg s^{-1} , assuming these sources are within the Circinus galaxy. The fact that all sources (with the possible exceptions of A, B and H) have observed column densities in excess of the Galactic column is consistent with them being in the Circinus galaxy. The luminosity of the most luminous of these sources corresponds to the Eddington luminosity of an $80 M_{\odot}$ black-hole.

Significant (at $> 90\%$ confidence) improvements in the fits to two sources are obtained when we include either one or two narrow ($\sigma = 10$ eV) Gaussian emission lines. The best-fit line energies and observed fluxes are given in Table 6. The equivalent widths are calculated with respect to the observed (absorbed) continuum. The presence of strong emission lines in three sources (F, G, and J) was claimed by Sambruna et al. (2001a), and it is worth comparing our results with theirs (see also Bauer et al. 2001). Source G (source 2 from Sambruna et al. 2001a) is relatively faint, and it

is therefore possible that the lines present in our data at 1.0 and 2.8 keV correspond to the lines at 1.2 and 2.3 keV found by Sambruna et al. (2001a). We note that there is no evidence for Fe $K\alpha$ line emission in this source, which indicates that there is little or no contamination from the nucleus. Sources F and J are piled-up in our 3.2s frame time data, and so we have only used the 0.4s frame time data, which has a total good time interval of 4913s. Our spectra (Figure 10) should be of worse quality than those obtained from the zero order image in the HETGS observation above $\gtrsim 2$ keV. Thus, it is not surprising that we did not detect any of the lines identified by Sambruna et al. (2001a) in sources F and J, although we have a marginal detection of a line at 2.7 keV in source F (source 6 of Sambruna et al. 2001a). The upper limits from our data for the equivalent widths of the emission lines identified by Sambruna et al. (2001a) in sources F and J are in the range ~ 50 to ~ 150 eV (and an upper limit of 1.3 keV for a line at 6.9 keV in source F is obtained from a spectral analysis of the unbinned data using the C-statistic).

4. Comparison with other Wavelengths

The [OIII] $\lambda 5007$ and $H\alpha$ emission line images from Veilleux & Bland-Hawthorn (1997) are compared with the X-ray image in the 0.5–8 keV band in Figure 11. During the optical observations, the seeing averaged FWHM $\simeq 1''$, which is similar to the spatial resolution of the X-ray image. As mentioned by Veilleux & Bland-Hawthorn (1997), the $H\alpha$ line flux was integrated over a specific velocity range to emphasize the outflow structure and to de-emphasize emission from the circumnuclear starburst. Regardless, the $H\alpha$ image shows the starburst ring plus some outflowing gas, while the [OIII] image is dominated by the high excitation, outflowing gas. The large-scale diffuse X-ray emission toward the NW of the nucleus is strongly correlated with the high excitation gas evident in the [OIII] image. Thus, the X-ray emission may be associated with a hot radiatively driven wind, shocks driven by mass outflow, or highly excited photoionized gas (see Section 5). However, the large-scale diffuse X-ray emission toward the SW is only loosely correlated with the $H\alpha$ line emission and not at all with the [OIII]. This emission extends some $15''$ from the nucleus, a similar scale to the ring of HII regions, so the X-ray emission here may be associated with the starburst.

5. Discussion

5.1. Nuclear Emission

The *Chandra* ACIS spectrum of the Circinus nucleus is dominated by a hard ($\Gamma \sim 0$) power-law continuum and strong Fe $K\alpha$ line emission, characteristic of a Compton reflection continuum. A likely scenario is that the nuclear continuum, evident in the *BeppoSAX* data above $\simeq 10$ keV, is Compton reflected from the far side of the putative dense torus. If the ionization cone is collimated by the torus, then the observed half-opening angle of the cone, $\theta \simeq 45^\circ$ (Wilson et al. 2000),

corresponds to a torus solid angle $\Omega/4\pi = \cos\theta = 0.7$. This is larger than the solid angle measured from the *BeppoSAX* data ($\Omega/4\pi \simeq 0.1$; Matt et al. 1999), which suggest that only a small fraction of the inner face of the torus is visible directly. For a torus solid angle of $\Omega/4\pi = 0.1$, the unobscured nuclear flux must be of order $1.2 \times 10^{42} \text{ erg s}^{-1}$ in the 2–10 keV band, which is within the range of luminosities inferred from the *BeppoSAX* data (3.4×10^{41} – $1.7 \times 10^{42} \text{ erg s}^{-1}$; Matt et al. 1999). Thus, it is likely that the Compton reflection and Fe K α fluorescence line observed from the nucleus originate in an almost edge-on torus. Such an orientation would be consistent with the strong water vapor masers in the nucleus of the Circinus galaxy (e.g. Gardner & Whiteoak 1982).

5.2. Large Scale X-ray Emission

A small fraction of the hard (3–10 keV) X-ray emission in the Circinus field extends hundreds of parsecs NW from the nucleus, and is cospatial with the regions of high excitation gas evident in the [OIII] image (Figure 11). The 2–10 keV observed flux and luminosity of this gas are $7.4 \times 10^{-14} \text{ erg cm}^{-2} \text{ s}^{-1}$ and $1.4 \times 10^{38} \text{ erg s}^{-1}$, respectively. The X-ray spectrum of the NW extension above 3 keV is similar to that observed in the nucleus, and is marginally consistent with the putative unobscured nuclear spectrum. It is worthwhile to consider whether this component could be electron scattered nuclear flux. The scattered X-ray luminosity, L_{scat} , is given as

$$L_{\text{scat}} = L_{\text{int}} \frac{\Omega}{4\pi} \tau_{\text{scat}},$$

where L_{int} is the intrinsic nuclear luminosity, Ω is the solid angle subtended by the scatterer as viewed from the nucleus, and τ_{scat} is the optical depth through the scattering gas. The unabsorbed 2–10 keV nuclear luminosity is in the range 1.2×10^{41} to $1.7 \times 10^{42} \text{ erg s}^{-1}$ (Matt et al. 1999), and the 2–10 keV luminosity of the scattered emission, after correcting for absorption and the contribution from nuclear light scattered by the telescope mirrors (Section 3.3.1), is $\simeq 7 \times 10^{37} \text{ erg s}^{-1}$. Assuming a half-opening angle of $\theta \simeq 45^\circ$ for the ionization cone, the solid angle subtended by the scatterer is $\Omega/4\pi = \frac{1}{2}(1 - \cos\theta) = 0.15$, so the column density of electrons through the scattering gas is in the range 4×10^{20} to $2 \times 10^{21} \text{ cm}^{-2}$. This is smaller than any intrinsic absorbing column associated with the large-scale emission to the NW (Table 3) and thus does not require the scattering gas to be very highly ionized for the scattered X-rays to escape.

The thermal component in the spectrum of the NW extension has a temperature of $T \simeq 7 \times 10^6 \text{ K}$ and an emission measure of $n_e^2 V \simeq 6 \times 10^{61} \text{ cm}^{-3}$, which yields $n_e \simeq 0.15 \text{ cm}^{-3}$ assuming a volume $V = 2.8 \times 10^{63} \text{ cm}^3$ for the emitting region. The pressure and cooling time of the X-ray emitting gas are then $n_e kT \simeq 1.5 \times 10^{-10} \text{ erg cm}^{-3}$ and $n_e kTV/L_X \simeq 7 \times 10^7 \text{ years}$, respectively, assuming a 0.5–10 keV luminosity, after correcting for absorption, of $L_X \simeq 2.0 \times 10^{38} \text{ erg s}^{-1}$. The velocity gradients across the [OIII] emission line images are of order 100–200 km s^{-1} (Veilleux & Bland-Hawthorn 1997), indicating that the gas is too hot to have been heated in situ by shocks with velocities in this range. Thus, a plausible explanation is that the X-ray emitting gas is associated with a wind outflowing from the nucleus. The alternative is that the X-ray emitting gas is photo-

ionized by the nucleus and thus mostly emission lines from a much cooler plasma. Higher spectral resolution observations are needed to distinguish these two quite different models.

5.3. Compact X-ray Sources

The compact X-ray sources within $10''$ (190 pc) of the nucleus are most likely to be X-ray binary systems or supernova remnants within the starburst rings of the Circinus galaxy. The measured column densities for at least three of the closest objects (sources C, E, and G) are above the Galactic value, presumably because of the large amount of molecular gas associated with the starburst disk. The association of the other sources with the Circinus galaxy is less certain. Source F is close to, but not coincident with, a patch of $H\alpha$ emission $\simeq 27''$ south of the nucleus, possibly an H II region in a spiral arm of the galaxy (Elmouttie et al. 1998). This X-ray source has a hard X-ray spectrum and presumably is an X-ray binary; it may show a weak extension to the SW (Figure 1). Sambruna et al. (2001a) and Bauer et al. (2001) report periodic variability in source J, with the flux decreasing to zero every $\simeq 27$ ks. Assuming source J is within the Circinus galaxy, its hard spectrum and high luminosity would suggest a massive ($\gtrsim 80 M_{\odot}$) black-hole in an X-ray binary as the likely origin for the X-ray emission. The fact that the column density to source J is larger than the Galactic column (Table 5) supports an association with Circinus. Alternatively, if source J is within our own galaxy, it might be associated with a magnetic Cataclysmic Variable system.

6. Conclusions

The main results of our *Chandra* X-ray observations of the Circinus galaxy are as follows. i) The nucleus contains a bright, compact X-ray source plus emission extended by $\simeq 60$ pc in the general direction of the ionization cone. Our observations confirm that the observed nuclear spectrum arises through reflection of a hard X-ray source by neutral matter with a high column density. Our emission-line fluxes are generally consistent with those measured by Sambruna et al. (2001b) with much higher spectral resolution grating observations. The Fe K α emission is extended by up to 200 pc. ii) There is also large scale (up to 600 pc from the nucleus), extended emission both along the plane of the galaxy disk (i.e. to the NE and SW) and perpendicular to it (i.e. to the NW). The spectrum of the extended emission along the galaxy disk may be described as emission from gas in collisional equilibrium with $kT \sim 0.6$ keV and may be associated with the starburst ring. There is no significant hard component in excess of that expected by telescope-mirror scattering of the bright nuclear source. The absorbing column density to gas in the galaxy disk exceeds that from our own galaxy, indicating significant intrinsic absorption by the disk of Circinus. The large-scale gas extending perpendicular to the disk is closely correlated with the high excitation optical-line emitting gas. The spectrum suffers no intrinsic absorption since the gas is on the near side of the Circinus galaxy disk. The soft component may be a thermal gas

with $kT \sim 0.6$ keV or may be cooler and photo-ionized by the Seyfert nucleus. Hard emission is detected which appears to exceed that expected from scattering of nuclear light by the telescope mirrors. We suggest that this hard component results from scattering of nuclear light into our line of sight by electrons in an ionized wind. iii) Ten compact X-ray sources are detected in the inner ~ 1 kpc of the galaxy. Their spectra may be described as power-laws with a significant amount of intrinsic absorption, consistent with their location in the inner disk of Circinus, which is known to be rich in molecular gas. The source luminosities range from 4×10^{37} to 1.0×10^{40} erg s $^{-1}$. The most luminous source (J) exhibits a hard spectrum and is apparently an X-ray binary in Circinus with a black-hole mass exceeding $80 M_{\odot}$.

We thank Sylvain Veilleux and Alessandro Marconi for providing their optical images of Circinus in computer readable format. This research made use of funding through NASA grant NAG-81027.

REFERENCES

- Anders, E., & Grevesse, N. 1989, *Geochimica et Cosmochimica Acta*, 53, 197
- Band, D. L., Klein, R. I., Castor, J. I., & Nash, J. K. 1990, *ApJ*, 362, 90
- Bauer, F. E., et al. 2001, *BAAS*, 32, 1536
- Cash, W. 1979, *ApJ*, 228, 939
- Chartas, G., et al. 2000, *ApJ*, 542, 655
- Elmouttie, M., Koribalski, B., Gordon, S., Taylor, K., Houghton, S., Lavezzi, T., Haynes, R., & Jones, K. 1998, *MNRAS*, 297, 49
- Freeman, K. C., Karlsson, B., Lyngå, G., Burrell, J. F., van Woerden, H., & Goss, W. M. 1977, *A&A*, 55, 445
- Garmire, G. P., et al. 2000, *ApJS*, submitted
- Gardner, F. F., & Whiteoak, J. B. 1982, *MNRAS*, 201, 13P
- Gondek, D., Zdziarski, A. A., Johnson, W. N., George, I. M., McNaron-Brown, K., Magdziarz, P., Smith, D., & Gruber, D. E. 1996, *MNRAS*, 282, 646
- Greenhill, L. J. 2001, in *Proceedings of the 5th EVN Symposium*, edited by J. Conway, A. Polatidis, and R. Booth (CUP, Cambridge), in press (astro-ph/0010277)
- Guainazzi, M., Matt, G., Antonelli, L. A., Bassani, L., Fabian, A. C., Maiolino, R., Marconi, A., Fiore, F., Iwasawa, K., & Piro, L. 1999, *MNRAS*, 310, 10

- Krolik, J. H. & Kallman, T. M. 1987, *ApJ*, 320, L5
- Magdziarz, P. & Zdziarski, A. A. 1995, *MNRAS*, 273, 837
- Maiolino, R., Krabbe, A., Thatte, N., & Genzel, R. 1998, *ApJ*, 493, 650
- Marconi A., Moorwood A. F. M., Origlia L., & Oliva E. 1994, *The ESO Messenger*, 78, 20
- Matt, G., Fiore, F., Perola, G. C., Piro, L., Fink, H. H., Grandi, P., Matsuoka, M., Oliva, E., & Salvati, M. 1996, *MNRAS*, 281, L69
- Matt, G., et al. 1999, *A&A*, 341, L39
- Mewe, R., Kaastra, J. S., Liedahl, D. A. 1995, *Legacy* 6, 16
- Morrison, R. & McCammon, D. 1983, *ApJ*, 270, 119
- Netzer, H., Turner, T. J., & George, I. M. 1998, *ApJ*, 504, 680
- Nousek, J. A. & Shue, D. R. 1989, *ApJ*, 342, 1207
- Oliva, E., Marconi, A., Cimatti, A., & di Serego Alighieri, S. 1998, *A&A*, 329, L21
- Sako, M., Kahn, S. M., Paerels, F., & Liedahl, D. A. 2000, *ApJ*, 542, 684
- Sambruna, R. M., Brandt, W. N., Chartas, G., Netzer, H., Kaspi, S., Garmire, G. P., Nousek, J. A., & Weaver, K. A. 2001a, *ApJ*, 546, L9
- Sambruna, R. M., Netzer, H., Kaspi, S., Brandt, W. N., Chartas, G., Garmire, G. P., Nousek, J. A., & Weaver, K. A. 2001b, *ApJ*, 546, L13
- Veilleux, S., & Bland-Hawthorn, J. 1997, *ApJ*, 479, L105
- Wilson, A. S., Shopbell, P. L., Simpson, C., Storchi-Bergmann, T., Barbosa, F. K. B. & Ward, M. J. 2000, *AJ*, 120, 1325
- Zdziarski, A. A., Johnson, W. N., Done, C., Smith, D., & McNaron-Brown, K. 1995, *ApJ*, 438, L63

Fig. 1.— An image of the central $1'2 \times 1'2$ region of the Circinus field in the 0.5–8 keV band. The image has been smoothed with a Gaussian profile of width $\sigma = 1$ pixel ($= 0''.5$). The contours indicate 2, 4, 8, 16, 64, 256, and 1024 cts pixel $^{-1}$ in the smoothed image. Letters refer to the sources discussed in the text and listed in Table 1.

Fig. 2.— An unsmoothed image of the circumnuclear region in the 0.5–8 keV band. Crosses and letters mark the locations of discrete sources found by the WAVDETECT algorithm. The vertical bar indicates the conversion from grey scale to cts pixel $^{-1}$.

Fig. 3.— A radial profile of the circumnuclear region in the 0.5–8 keV band (obtained from the 0.4s frame time observation) after excluding the contribution of compact X-ray sources. The data and telescope PSF are shown as the solid- and dashed-line histograms, respectively, and 1 pixel $= 0''.5$.

Fig. 4.— The distribution of Fe K α line emission in the Circinus galaxy. The image has been smoothed with a Gaussian profile of width $\sigma = 1$ pixel ($= 0''.5$). Contours are drawn at -1 , -0.5 (dashed), 0.5, 1, 2, 4, 8, 16, 32, 64, and 128 cts pixel $^{-1}$ in the smoothed image. The crosses mark the positions of the sources detected in the 0.5–8 keV band with the WAVDETECT algorithm (Section 3.1). The features in the extreme upper left (near sources I and J) reflect residuals errors in the subtraction of the continuum rather than real Fe K α emission.

Fig. 5.— The nuclear spectrum of Circinus. The upper panel shows the data and folded model comprising the best-fit absorbed power-law continuum plus Fe K α emission line (model 1; Section 3.2.2). The lower panel shows the ratio of data to the model. Several prominent emission lines are seen in the spectrum at energies corresponding to neutral or ionized species of Ne, Mg, Si, S, and Fe K β (see Table 2).

Fig. 6.— An optical continuum image (contours) of the Circinus galaxy at 7000Å (from Marconi et al. 1994) superposed on the *Chandra* X-ray image (greyscale) in the 0.5–8 keV band, smoothed with a Gaussian profile of width $\sigma = 1$ pixel ($= 0''.5$). The vertical bar indicates the conversion from grey scale to cts pixel $^{-1}$ in the X-ray image. Contours are drawn at 0.9, 1.1, 1.3, 1.65, 2.2, 3.3, 5.5, 11.0, and 22.0×10^{-18} erg cm $^{-2}$ s $^{-1}$ Å $^{-1}$ pixel $^{-1}$ in the optical image.

Fig. 7.— An image of an $\simeq 1' \times 1'$ region of the Circinus field in the 0.5–8 keV band. The image has been smoothed with a Gaussian profile of width $\sigma = 1$ pixel ($= 0''.5$). The crosses mark the locations of the discrete sources found by the WAVDETECT algorithm. The solid black lines show regions from which spectra of the diffuse X-ray emission were extracted. The vertical bar indicates the conversion from grey scale to cts pixel $^{-1}$.

Fig. 8.— The spectrum of the NW large scale extended emission in Circinus. The data are shown together with the best-fit absorbed thermal bremsstrahlung plus power-law continuum model (model B+P; see Table 3 and Section 3.3.1). The vertical lines mark the best-fit energies of the emission lines present in the spectrum.

Fig. 9.— The spectrum of the SW large scale extended emission in Circinus. The data are shown together with the best-fit absorbed thermal bremsstrahlung plus power-law continuum model (model B+P; see Table 4 and Section 3.3.2). The emission above 3 keV, including the observed Fe $K\alpha$ line, is believed not to be real, but rather represents nuclear emission scattered into the region by the telescope mirrors (Section 3.3.2).

Fig. 10.— Short (0.4s; triangles) and long (3.2s; crosses) frame time spectra of two of the ten compact X-ray sources found in the central $\sim 1' \times 1'$ region of the Circinus field. The upper panel shows the data and folded model comprising the best-fit absorbed power-law continuum (see Table 5 and Section 3.4). The lower panel shows the ratio of data to the model. The hard ($\gtrsim 7$ keV) X-ray emission in excess of the absorbed power-law is a consequence of pileup in the 3.2s frame time data. (a) Source F. (b) Source J.

Fig. 11.— Optical emission line images (from Veilleux & Bland-Hawthorn 1997) of the Circinus galaxy (contours) superposed on the *Chandra* X-ray image (greyscale) in the 0.5–8 keV band, smoothed with a Gaussian profile of width $\sigma = 1$ pixel ($= 0''.5$). The vertical bar represents the relation between shade and cts pixel $^{-1}$ in the X-ray image. (a) [OIII] $\lambda 5007$. Contours represent 50, 150, 300, 600, and 1200 cts pixel $^{-1}$. (b) Blueshifted (between -150 and 0 km s $^{-1}$) H α . Contours represent 25, 50, 100, 250, 500, 1000, and 2500 cts pixel $^{-1}$.

Table 1. Bright sources in the inner part of the Circinus field.

Source	RA(2000)	Dec(2000)	Count rate ^a
A	14 13 05.54	-65 20 31.6	1.9 ± 0.3
B	14 13 09.15	-65 20 17.7	5.3 ± 0.6
C	14 13 09.60	-65 20 22.1	3.2 ± 0.8
D	14 13 09.94	-65 20 21.0	330 ± 8
E	14 13 10.00	-65 20 29.8	6.0 ± 0.6
F	14 13 10.05	-65 20 44.8	102 ± 5
G	14 13 10.29	-65 20 18.0	25.9 ± 1.2
H	14 13 10.37	-65 20 22.7	8.8 ± 0.7
I	14 13 12.20	-65 20 07.4	10.5 ± 0.7
J	14 13 12.25	-65 20 14.0	341 ± 9
K	14 13 12.54	-65 20 52.8	6.9 ± 0.5

^a0.1–10 keV count rate expressed in units of 10^{-3} counts s⁻¹

Table 2. Emission lines from the nucleus.

Energy ^a (keV)	Line(s)	Flux ^b (10^{-5} ph cm $^{-2}$ s $^{-1}$)	EW ^c (eV)	Flux ^d (10^{-5} ph cm $^{-2}$ s $^{-1}$)	Ratio ^e
1.211	Ne x Ly β	$1.35^{+1.3}_{-1.2}$	130^{+130}_{-110}	0.25 ± 0.15	5.4 ± 6.2
1.332	Mg xi f	$0.3^{+1.6}_{-0.3}$	30^{+160}_{-30}	0.34 ± 0.16	0.85 ± 4.7
1.341	Mg xi i	< 2.0	< 215	0.26 ± 0.13	$\lesssim 7.7$
1.352	Mg xi r	$0.8^{+1.2}_{-0.8}$	80^{+130}_{-80}	0.58 ± 0.17	1.3 ± 2.1
1.471	Mg xii Ly α	$< 0.43^f$	< 49	0.65 ± 0.16	$\lesssim 0.66^f$
1.578	Mg xi 1s3p–1s 2	$0.22^{+0.66}_{-0.22}$	28^{+84}_{-28}	0.19 ± 0.13	1.2 ± 3.6
1.741	Mg xii Ly β + Si ii–vi K α	$1.89^{+0.92}_{-0.69}$	260^{+130}_{-100}	0.86 ± 0.17	2.2 ± 1.2
1.841	Si xiii f + Mg xii Ly γ	< 1.5	< 230	1.05 ± 0.18	$\lesssim 1.4$
1.863	Si xiii r	$1.6^{+0.9}_{-1.6}$	265^{+140}_{-255}	0.87 ± 0.16	1.9 ± 1.8
2.006	Si xiv Ly α	$< 0.37^f$	< 63	0.64 ± 0.15	$\lesssim 0.58^f$
2.313	S ii–xii K α	$1.56^{+0.81}_{-0.82}$	270 ± 140	0.29 ± 0.32	5.4 ± 6.6
2.383	Si xiv Ly β + S xii 1s2s 2 2p 2 –1s 2 2s 2 2p	< 1.0	< 170	0.48 ± 0.37	$\lesssim 2.1$
2.412	S xiv 1s2s2p–1s 2 2s	< 1.5	< 260	0.28 ± 0.27	$\lesssim 5.4$
2.433	S xv f	$1.2^{+1.5}_{-1.2}$	200^{+260}_{-200}	0.56 ± 0.29	2.1 ± 2.9
2.458	S xv r	$0.9^{+1.5}_{-0.9}$	150^{+260}_{-150}	0.85 ± 0.36	1.0 ± 1.8
2.624	S xvi Ly α	$0.36^{+0.58}_{-0.36}$	60^{+100}_{-60}	0.22 ± 0.23	1.6 ± 3.1
2.882	S xv 1s3p–1s 2	$0.23^{+0.57}_{-0.23}$	36^{+89}_{-36}	0.21 ± 0.23	1.1 ± 3.0
2.960	Ar ii–xi K α	$0.46^{+0.60}_{-0.46}$	69^{+90}_{-69}	0.6 ± 0.31	0.8 ± 1.1
3.268	Ar xviii Ly α	$0.10^{+0.52}_{-0.10}$	14^{+73}_{-14}	0.40 ± 0.24	0.25 ± 1.3
3.683	Ca ii–xiv K α	$0.76^{+0.59}_{-0.60}$	92^{+71}_{-73}	0.38 ± 0.21	2.0 ± 1.9
3.917	Ar xviii Ly β	< 0.50	< 57	0.41 ± 0.26	$\lesssim 1.2$
4.758		< 0.28	< 27	0.52 ± 0.29	$\lesssim 0.54$
5.166		$0.22^{+0.71}_{-0.22}$	19^{+61}_{-19}	1.02 ± 0.40	0.22 ± 0.70
5.993		$0.49^{+0.96}_{-0.49}$	38^{+74}_{-38}	1.45 ± 0.54	0.34 ± 0.67
6.382 ^g	Fe ii–xvii K α	$29.4^{+3.3}_{-3.9}$	2250^{+260}_{-300}	30.5 ± 1.7	0.96 ± 0.14
6.656	Fe xxv r	< 0.94	< 69	2.73 ± 1.10	$\lesssim 0.34$
7.030	Fe ii–xvii K β	2.25 ± 1.7	210 ± 160	6.8 ± 1.5	0.33 ± 0.26

^aEmission line energy measured by Sambruna et al. (2001b)

^bLine flux from the present data

^cEquivalent width with respect to the observed continuum from the present data

^dLine flux from the HETGS spectrum (Sambruna et al. 2001b)

^eRatio of the ACIS (present data) to HETGS (Sambruna et al. 2001b) line fluxes; the larger error on the ACIS flux was used in calculating the uncertainty on the line ratio

^fUnreliable measurement due to structure in the instrumental response (see text)

^gLine energy measured in ACIS data

Table 3. Spectral fits to the NW large-scale extended emission.

Model ^a	Method ^b	kT_l^c (keV)	kT_h^d (keV)	Z^e (Z_\odot)	Γ^f	N_H^g (10^{21} cm^{-2})	F_X^h ($10^{-14} \text{ erg cm}^{-2} \text{ s}^{-1}$)	χ^2 (d.o.f.)
B+P	1	$0.187^{+0.090}_{-0.053}$	$1.96^{+0.47}_{-0.50}$	$6.7^{+0.6}_{-1.4}$	4.8	...
B+P	2	$0.137^{+0.036}_{-0.028}$	$2.60^{+0.52}_{-0.65}$	$8.7^{+0.45}_{-0.28}$	3.4	28.9 (22)
M1+P	1	...	$0.641^{+0.058}_{-0.066}$	1.0^{fixed}	$2.10^{+0.38}_{-0.39}$	$1.63^{+0.68}_{-0.70}$	4.2	...
M1+P	2	...	$0.630^{+0.063}_{-0.083}$	1.0^{fixed}	$2.33^{+0.55}_{-0.27}$	$1.88^{+0.72}_{-0.72}$	3.3	25.8 (22)
M2+P	1	...	$0.63^{+0.08}_{-0.10}$	$0.054^{+0.048}_{-0.023}$	$0.4^{+1.1}_{-1.2}$	$2.34^{+0.61}_{-0.57}$	7.1	...
M2+P	2	...	$0.63^{+0.08}_{-0.11}$	$0.052^{+0.047}_{-0.023}$	$0.0^{+0.5}_{-1.9}$	$2.36^{+0.60}_{-0.56}$	7.4	20.6 (21)
M1+M1	1	$0.664^{+0.097}_{-0.055}$	$5.3^{+4.1}_{-1.7}$	1.0^{fixed}	...	$0.74^{+0.45}_{-0.39}$	5.0	...
M1+M1	2	$0.655^{+0.053}_{-0.056}$	$4.1^{+2.3}_{-1.2}$	1.0^{fixed}	...	$0.72^{+0.41}_{-0.38}$	3.8	28.6 (22)
M2+M2	1	$0.61^{+0.09}_{-0.11}$	80_{-71}	$0.065^{+0.067}_{-0.028}$...	$2.21^{+0.68}_{-0.76}$	5.0	...
M2+M2	2	$0.62^{+0.07}_{-0.14}$	80_{-75}	$0.068^{+0.049}_{-0.032}$...	$2.12^{+0.84}_{-0.63}$	4.4	22.4 (21)

^aModel: B = bremsstrahlung; P = power-law; M1 = MEKAL with solar abundances (model valid for gas temperatures in the range 8 eV to 80 keV); M2 = MEKAL with variable abundances (model valid for gas temperatures in the range 8 eV to 80 keV)

^b1: spectral analysis of unbinned data using the C-statistic (Cash 1979); 2: spectral analysis of binned data using the χ^2 statistic

^cLow temperature thermal component

^dHigh temperature thermal component

^eMetal abundance

^fPhoton spectral index

^gMeasured column density

^hObserved 2–10 keV flux

Table 4. Spectral fits to the SW large-scale extended emission.

Model ^a	Method ^b	kT_l^c (keV)	kT_h^d (keV)	Z^e (Z_\odot)	Γ^f	N_H^g (10^{21} cm^{-2})	F_X^h ($10^{-14} \text{ erg cm}^{-2} \text{ s}^{-1}$)	χ^2 (d.o.f.)
B+P	1	$0.126^{+0.060}_{-0.029}$	$3.03^{+0.25}_{-0.18}$	$12.88^{+0.76}_{-0.48}$	4.6	...
B+P	2	$0.099^{+0.030}_{-0.022}$	$4.04^{+0.24}_{-0.20}$	$15.15^{+0.57}_{-0.52}$	3.0	42.5 (24)
M1+P	1	...	$0.628^{+0.053}_{-0.051}$	1.0^{fixed}	$2.30^{+0.46}_{-0.50}$	$5.41^{+0.97}_{-0.89}$	5.1	...
M1+P	2	...	$0.653^{+0.091}_{-0.063}$	1.0^{fixed}	$2.95^{+0.49}_{-0.44}$	$5.56^{+0.85}_{-0.77}$	3.3	30.5 (24)
M2+P	1	...	$0.643^{+0.059}_{-0.057}$	$0.099^{+0.052}_{-0.038}$	$-1.9^{+1.2}_{-1.5}$	$5.74^{+0.89}_{-0.78}$	18	...
M2+P	2	...	$0.68^{+0.14}_{-0.06}$	$0.088^{+0.052}_{-0.031}$	$-5.4^{+0.3}_{-4.0}$	$5.42^{+0.91}_{-0.11}$	76	21.4 (23)
M1+M1	1	$0.623^{+0.047}_{-0.043}$	11^{+32}_{-5}	1.0^{fixed}	...	$6.2^{+1.1}_{-1.2}$	6.8	...
M1+M1	2	$0.66^{+0.10}_{-0.05}$	$2.9^{+2.9}_{-0.7}$	1.0^{fixed}	...	$4.9^{+1.9}_{-0.6}$	4.1	42.6 (24)
M2+M2	1	$0.618^{+0.060}_{-0.066}$	80_{-65}	$0.14^{+0.10}_{-0.06}$...	$5.60^{+0.91}_{-0.84}$	6.0	...
M2+M2	2	$0.65^{+0.10}_{-0.06}$	80_{-78}	$0.109^{+0.083}_{-0.042}$...	$5.34^{+0.87}_{-0.85}$	4.6	28.1 (23)

^aModel: B = bremsstrahlung; P = power-law; M1 = MEKAL with solar abundances (model valid for gas temperatures in the range 8 eV to 80 keV); M2 = MEKAL with variable abundances (model valid for gas temperatures in the range 8 eV to 80 keV)

^b1: spectral analysis of unbinned data using the C-statistic (Cash 1979); 2: spectral analysis of binned data using the χ^2 statistic

^cLow temperature thermal component

^dHigh temperature thermal component

^eMetal abundance

^fPhoton spectral index

^gMeasured column density

^hObserved 2–10 keV flux

Table 5. Spectral fits to the bright sources in the field.

Source	A^a (10^{-6} ph cm $^{-2}$ sec $^{-1}$)	Γ^b	N_H^c (10^{21} cm $^{-2}$)	F_X^d (10^{-14} erg cm $^{-2}$ s $^{-1}$)	L_X^e (10^{37} erg s $^{-1}$)	χ^2 (d.o.f.)
A	6.1	$1.8^{+1.3}_{-0.9}$	8^{+12}_{-5}	2.0	4.1	0.89 (3)
B	8.8	$0.84^{+0.96}_{-0.76}$	13^{+11}_{-10}	14	28	5.6 (6)
C	44	$2.6^{+1.9}_{-1.3}$	20^{+20}_{-12}	4.0	9.7	14.6 (12)
E	89	$2.45^{+0.94}_{-0.66}$	31^{+16}_{-12}	8.8	23	2.2 (9)
F	280	$1.62^{+0.32}_{-0.26}$	$9.7^{+3.0}_{-2.0}$	120	230	28.2 (20)
G	310	$2.85^{+0.43}_{-0.33}$	$16.6^{+4.1}_{-3.0}$	19	46	41.5 (39)
H	7.8	$0.45^{+0.39}_{-0.31}$	$7.5^{+5.4}_{-3.6}$	26	51	8.5 (12)
I	23	$1.19^{+0.40}_{-0.27}$	$11.8^{+5.8}_{-3.8}$	20	41	10.6 (13)
J	820	$1.39^{+0.15}_{-0.14}$	$9.8^{+1.4}_{-1.1}$	510	1000	66.5 (70)
K	31	$1.84^{+0.70}_{-0.34}$	$14.1^{+8.2}_{-4.6}$	9.0	20	7.2 (7)

^aPhoton flux of the unabsorbed power-law continuum at 1 keV

^bPhoton spectral index

^cMeasured column density

^dObserved 2–10 keV flux

^eUnobscured 2–10 keV luminosity, assuming the source is in the Circinus galaxy (assumed distance = 4 Mpc)

Table 6. Emission lines from the bright sources in the field.

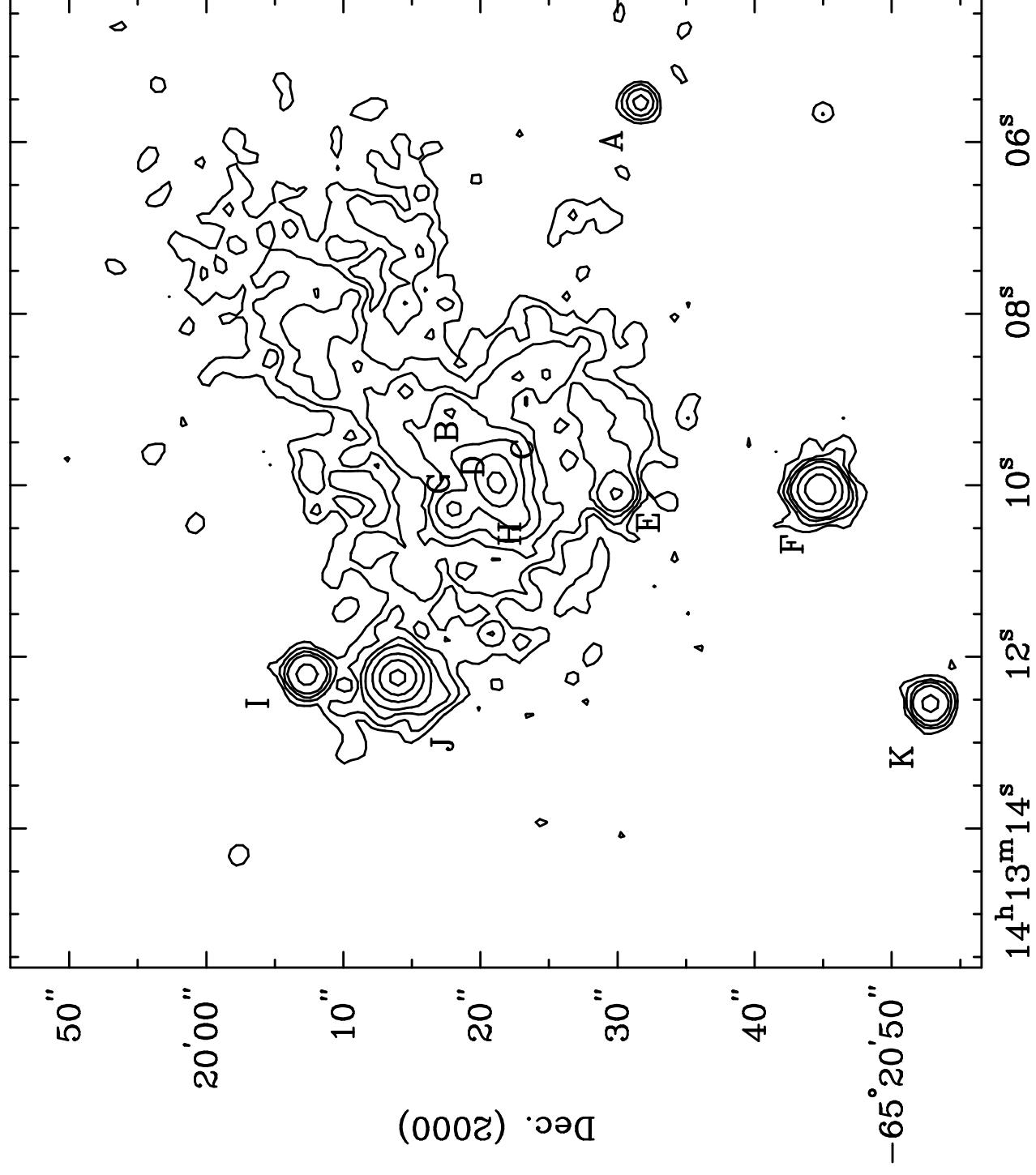
Source	Energy ^a (keV)	Line(s) ^b	Flux ^c (10^{-6} ph cm $^{-2}$ s $^{-1}$)	EW ^d (eV)	$\Delta\chi^2$ (d.o.f.)
G	$1.006^{+0.032}_{-0.028}$	Ne x Ly α	$1.18^{+0.76}_{-0.73}$	290^{+190}_{-180}	6.5 (2)
G	$2.773^{+0.031}_{-0.039}$	S xv 1s3p–1s 2	$2.4^{+0.9}_{-1.3}$	200^{+80}_{-110}	11.0 (2)
I	$4.02^{+0.09}_{-0.65}$	Ca II–XX	$1.06^{+0.89}_{-0.93}$	280^{+240}_{-250}	3.6 (2)

^aEmission line energy measured in the ACIS data

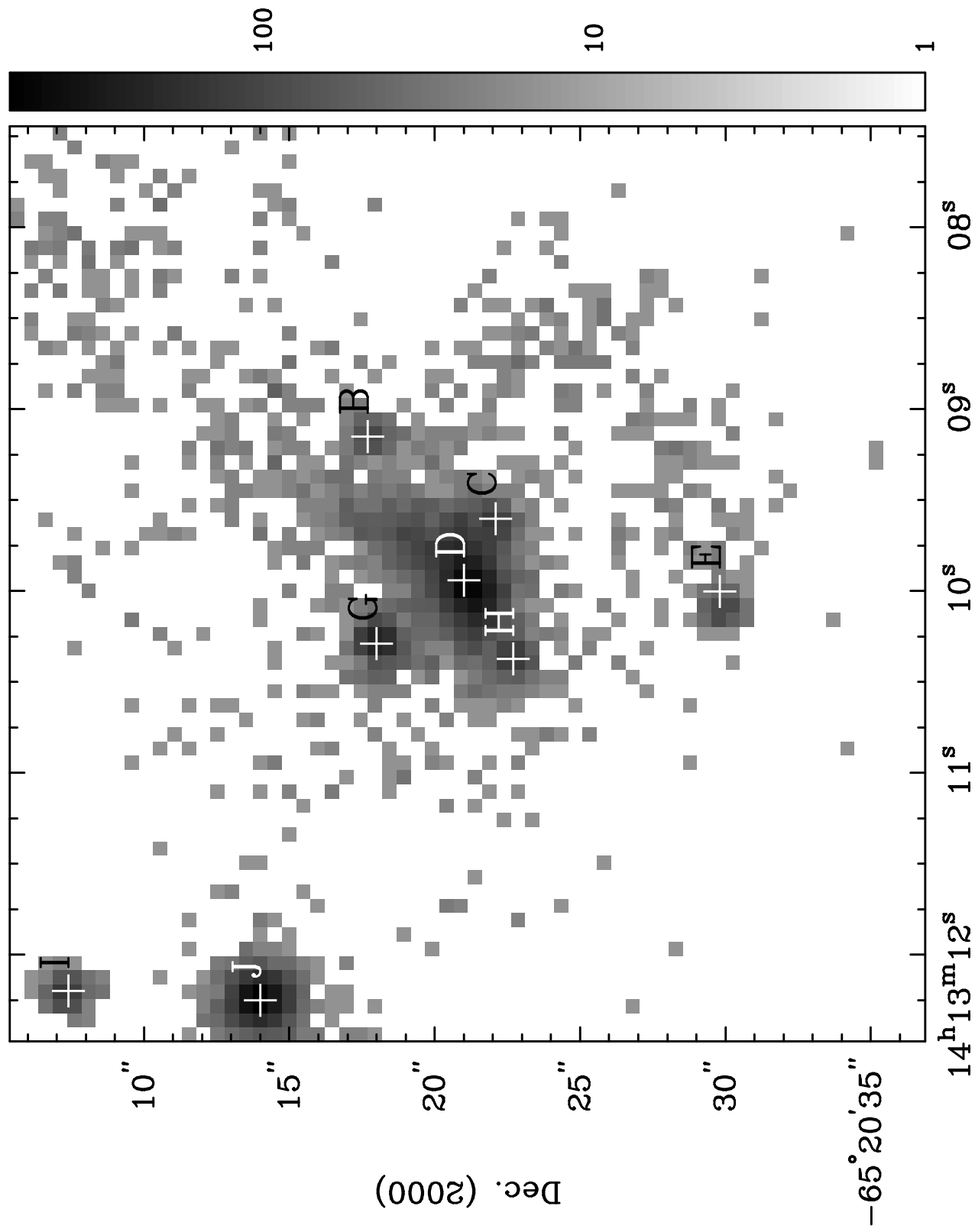
^bTentative identification

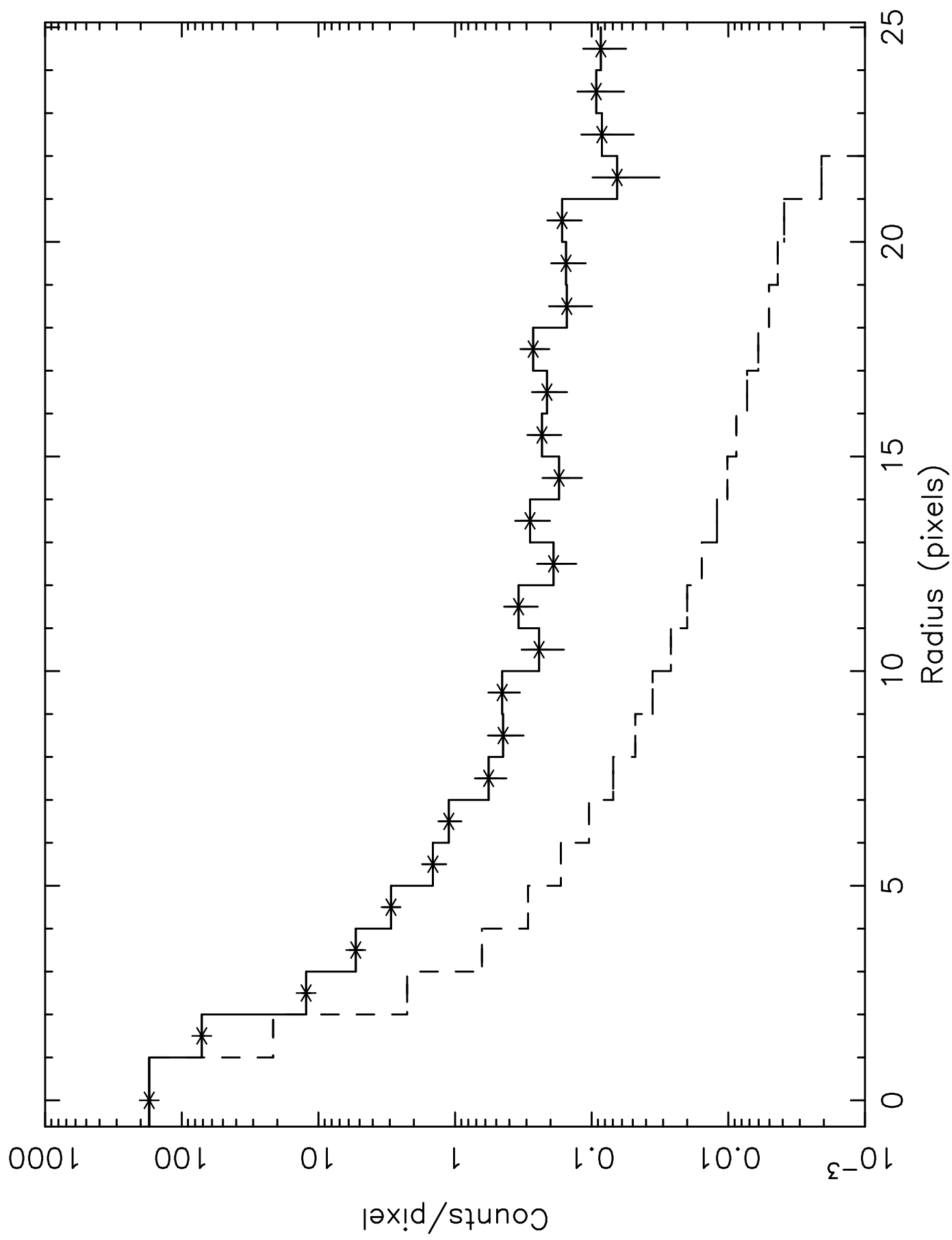
^cLine flux

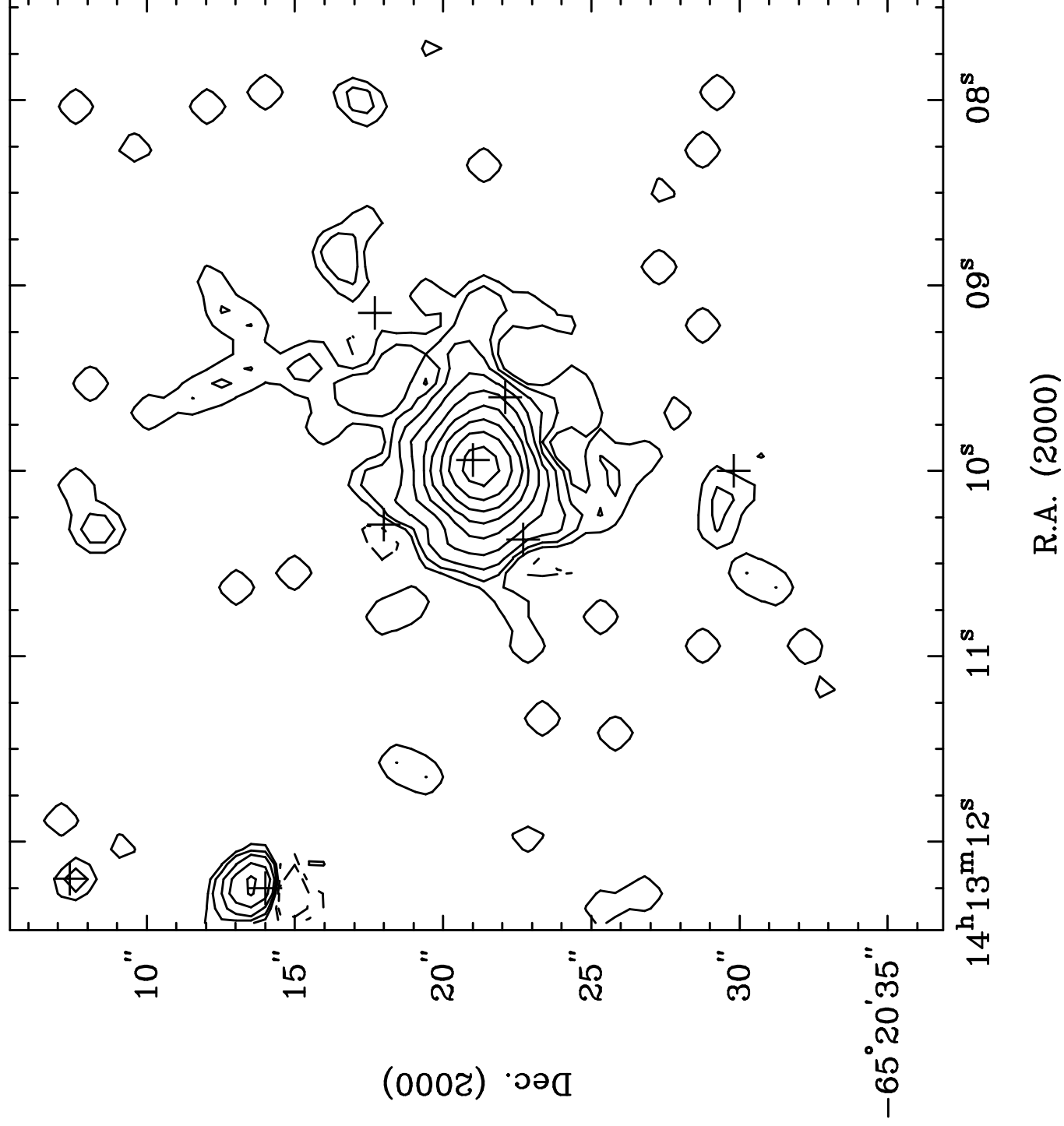
^dEquivalent width with respect to the observed continuum

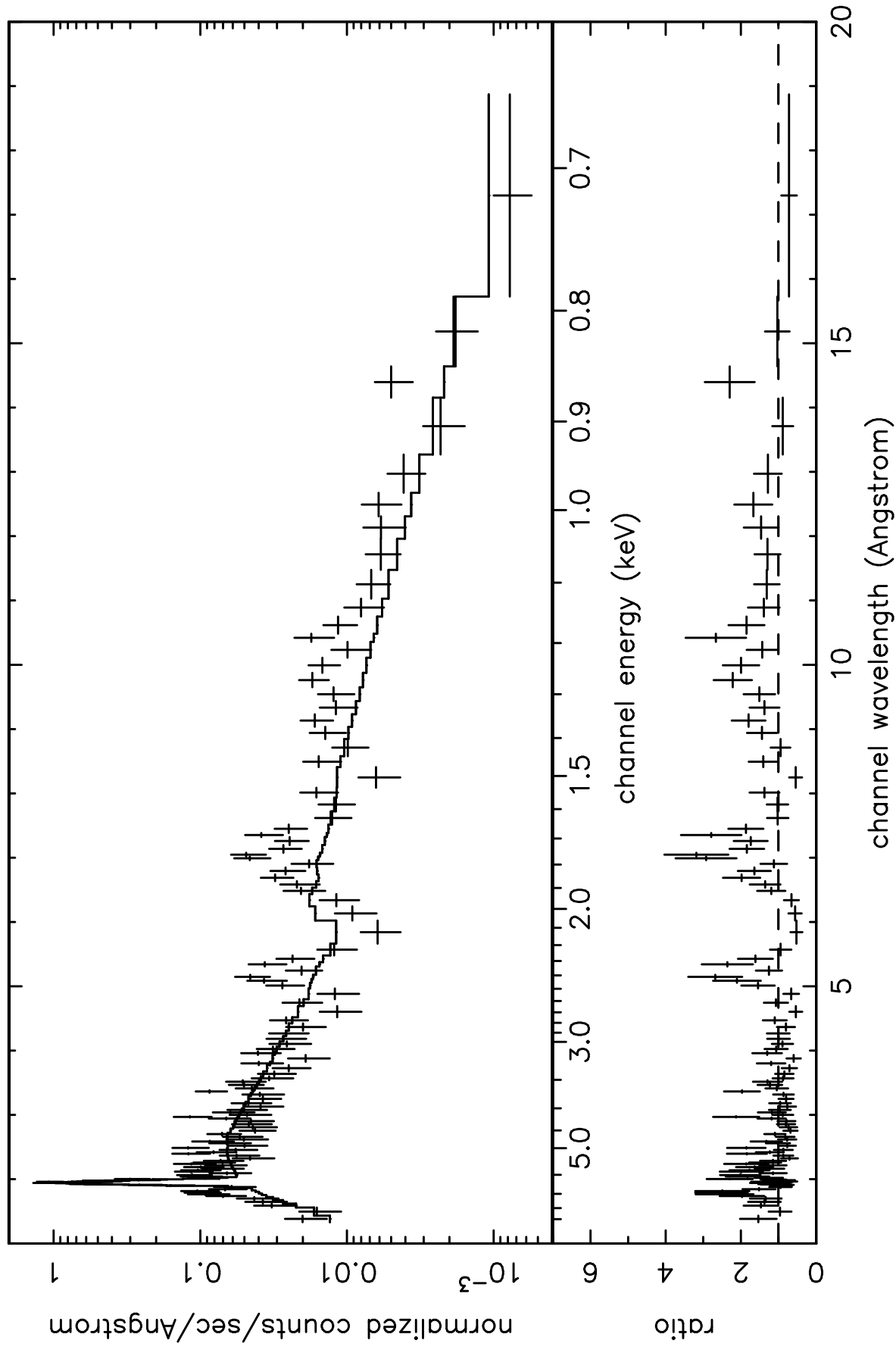


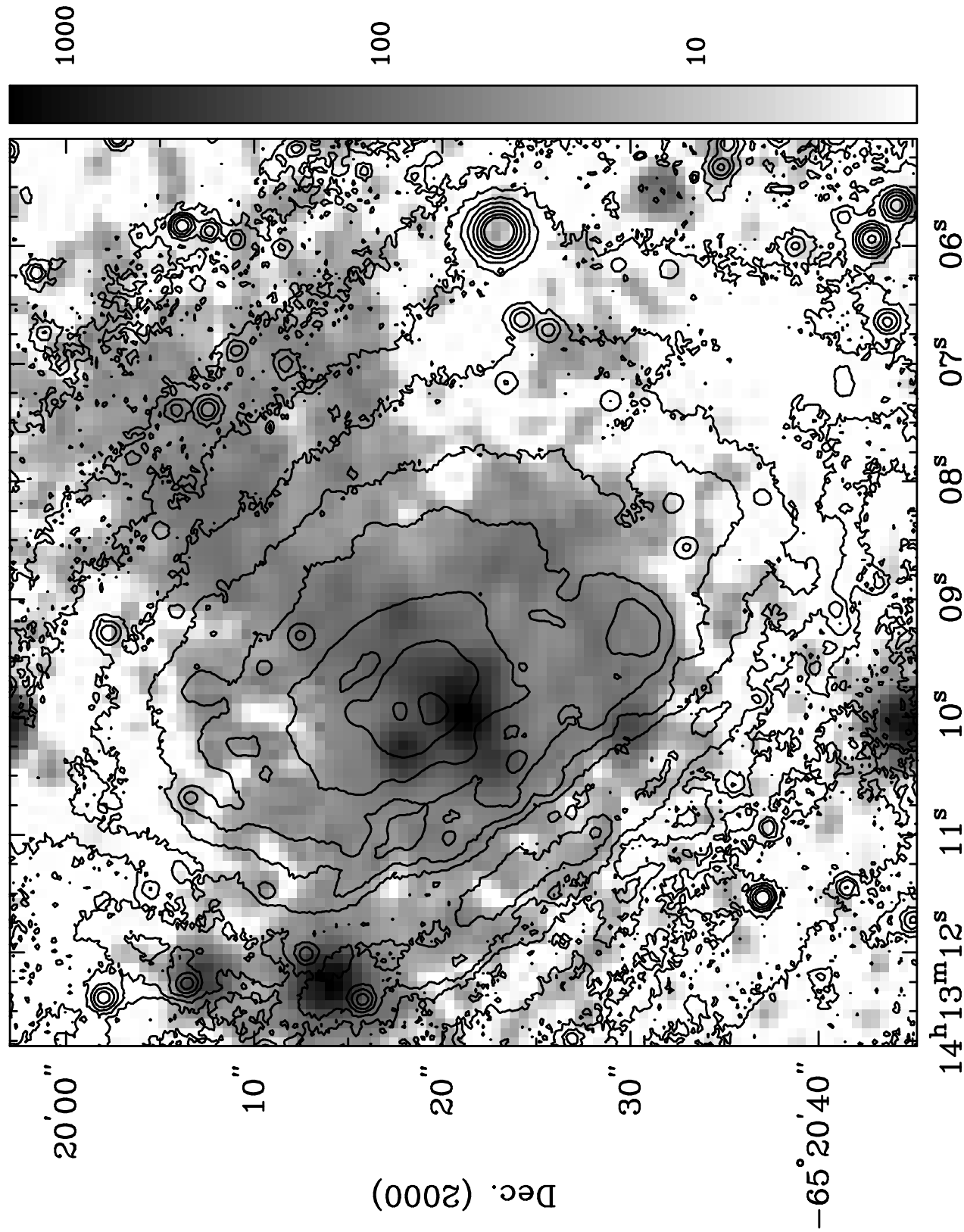
R.A. (2000)

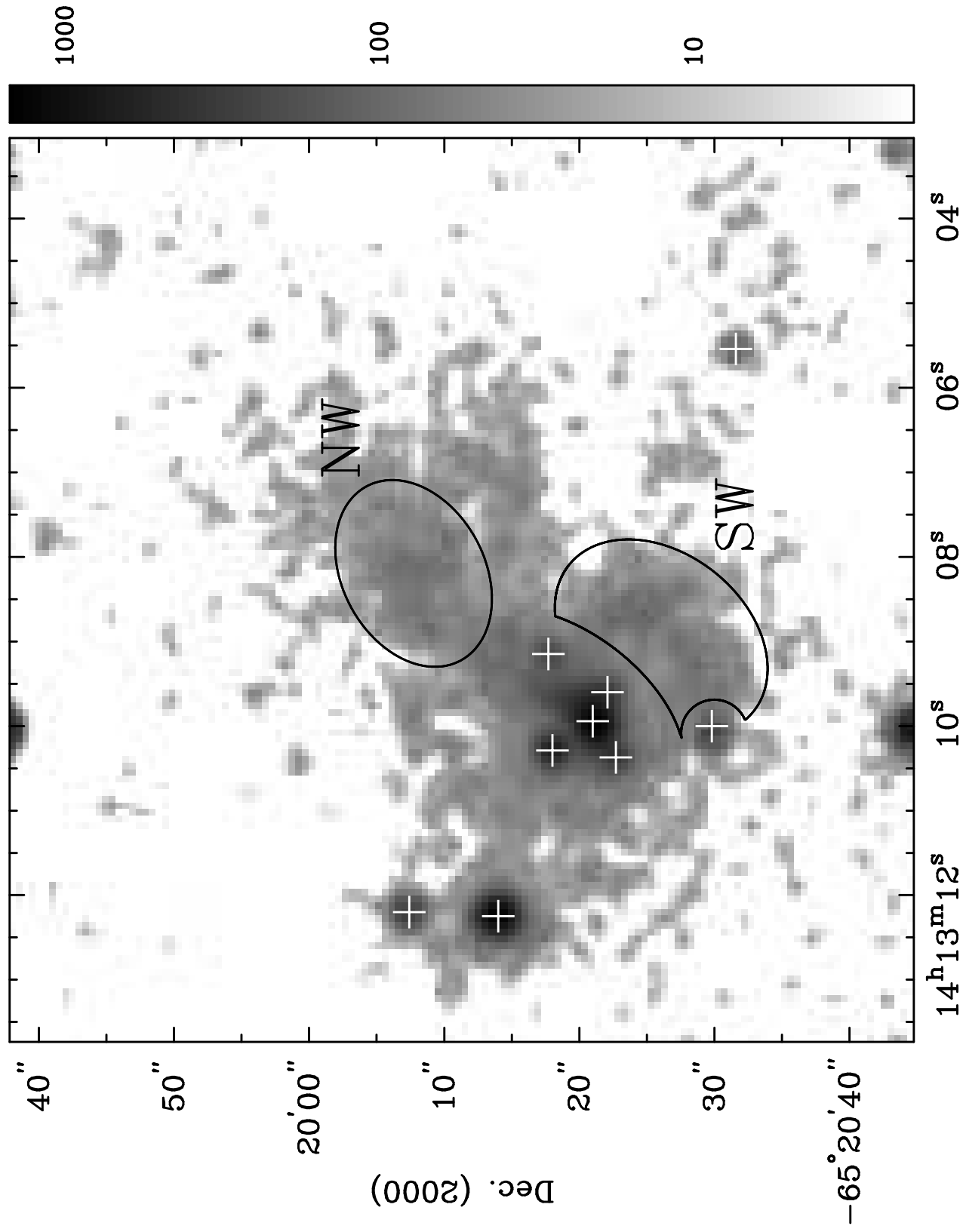












R.A. (2000)

